Simulation of transcranial magnetic stimulation in head model with morphologically-realistic cortical neurons

Aman S. Aberra[a], **Boshuo Wang**[b], **Warren M. Grill**[a,c,d,e], **Angel V. Peterchev**[a,b,c,e]

[a]Department of Biomedical Engineering, Duke University, Durham, NC 27708

[b]Department of Psychiatry and Behavioral Sciences, Duke University, Durham, NC 27710

[c]Department of Electrical and Computer Engineering, Duke University, Durham, NC 27708

[d]Department of Neurobiology, School of Medicine, Duke University, Durham, NC 27710

[e]Department of Neurosurgery, School of Medicine, Duke University, Durham, NC 27710

Abstract

Background: Transcranial magnetic stimulation (TMS) enables non-invasive modulation of brain activity with both clinical and research applications, but fundamental questions remain about the neural types and elements TMS activates and how stimulation parameters affect the neural response.

Objective: To develop a multi-scale computational model to quantify the effect of TMS parameters on the direct response of individual neurons.

Methods: We integrated morphologically-realistic neuronal models with TMS-induced electric fields computed in a finite element model of a human head to quantify the cortical response to TMS with several combinations of pulse waveforms and current directions.

Results: TMS activated with lowest intensity intracortical axonal terminations in the superficial gyral crown and lip regions. Layer 5 pyramidal cells had the lowest thresholds, but layer 2/3 pyramidal cells and inhibitory basket cells were also activated at most intensities. Direct activation of layers 1 and 6 was unlikely. Neural activation was largely driven by the field magnitude, rather than the field component normal to the cortical surface. Varying the induced current direction caused a waveform-dependent shift in the activation site and provided a potential mechanism for experimentally observed differences in thresholds and latencies of muscle responses.

Conclusions: This biophysically-based simulation provides a novel method to elucidate mechanisms and inform parameter selection of TMS and other cortical stimulation modalities. It also serves as a foundation for more detailed network models of the response to TMS, which may include endogenous activity, synaptic connectivity, inputs from intrinsic and extrinsic axonal projections, and corticofugal axons in white matter.

Keywords

finite element method; motor cortex; neuron models; simulation; transcranial magnetic stimulation

Introduction

Transcranial magnetic stimulation (TMS) is a technique for non-invasive modulation of brain activity using a magnetically-induced electric field (E-field) [1]. TMS is currently FDA-cleared for cortical mapping and the treatment of several psychiatric and neurological disorders, and it is under investigation for many other indications [2]. However, rational design and optimization of TMS is impeded by our limited understanding of its neural effects. Fundamental questions persist regarding the neural types and elements that are activated, the spatial extent of activation, and how spatial and temporal parameters of TMS determine threshold and site of activation, particularly when considering the complexities of human brain geometry. Obtaining insights into the cortical origin and mechanisms of the physiological response to TMS has proven difficult: electrical recording techniques in the brain or spinal cord are invasive and mostly reserved for animal studies, stimulus artifacts make it challenging to record during and immediately after the stimulus pulse, uncertainty remains about the stimulation focality, and experimental approaches have yet to produce a systematic assessment of the neural response across depths, positions, and cell types [3–5]. Optical imaging techniques, such as two-photon calcium imaging [6,7], can overcome some of these limitations, including the stimulus artifact and cell type identification, although action potential evoked calcium transients may be too long (>100 ms) to differentiate direct from indirect activation [8]. Still, these methods have thus far not been applied in studying TMS of humans and non-human primates.

Computational modeling is a powerful tool for investigating the mechanisms of TMS as well as for choosing stimulation parameters for more selective target engagement. Prior modeling efforts focused on calculating the spatial distribution of the E-field induced by TMS—typically using the finite element method (FEM) in head models derived from magnetic resonance imaging (MRI) data [9,10]. However, the spatial distribution of the E-field alone cannot predict the physiological effects of stimulation, and TMS can recruit distinct neural populations or elements based on different temporal dynamics of the E-field waveform (e.g., pulse shape, direction, width, and phase amplitude asymmetry) [11–15]. Therefore, the E-field must be coupled to neural models capturing the heterogeneity and spatial distribution of the underlying neural elements, as well as their membrane dynamics, to quantify the neural response to stimulation.

To simulate the neural response to TMS, cable theory was adapted and implemented in increasingly detailed compartmental neuron models [16–22]. These studies concluded that

axonal bends, branch points, and terminations are the most likely sites of action potential initiation by TMS. However, more recent studies suggest that TMS initiates action potentials at the cell body or axon initial segment [23–25]. Additionally, preliminary efforts to develop integrated models incorporating anatomically accurate E-fields with morphologically-realistic neurons lacked realistic axonal geometries, diversity of cell types, and/or morphological variability within cell types, resulting in limited insights into the neural activation mechanisms of TMS [20,24,26].

To address the questions about the interaction between TMS and neurons, we quantified the direct responses of cortical neurons to TMS-induced E-fields in a multi-scale model that incorporated cortical geometry, neural membrane dynamics, and axonal morphology, all of which are critical to model accurately the effects of TMS. We adapted recently published cortical neuron models from the Blue Brain Project [27,28] to the geometry of mature human cortical neurons, including excitatory and inhibitory cell types across all cortical layers, realistic axon morphologies, experimentally validated electrophysiological properties, and morphological variability within cell types [29]. We embedded these model neurons in cortical layers within the gray matter of a realistic FEM model of a human head. This level of detail and diversity of model neurons achieved a more biologically-plausible model of the direct cortical response to TMS than any previously published. We used this integrated model to simulate the neural response to TMS of primary motor cortex (M1) with several E-field directions and pulse shapes, including conventional and controllable pulse parameter TMS (cTMS). The simulations answered three key questions that have been controversial in the field: 1) which neural types and elements does TMS activate, 2) what is the site of activation by TMS of the motor cortex, and 3) how is the site of activation affected by E-field direction and waveform?

Methods

Neuron models

The neuron models were modified versions of the multi-compartmental, conductance-based models implemented by the Blue Brain Project [27,28] in the NEURON v7.4 simulation software [30]. The original models include 3D, reconstructed dendritic and axonal morphologies of cell types from all 6 cortical layers, with up to 13 different published Hodgkin-Huxley-like ion channel models in the soma, dendrites, and axon initial segment. Each cell type had five clones, which were generated by introducing stochastic variations in their dendritic and axonal geometries to reflect morphological diversity within cell type. Previously, we adapted a subset of these model neurons to the biophysical and geometric properties of adult, human cortical neurons and characterized their response to stimulation with exogenous E-fields [29]. These modifications included scaling the morphologies to account for age and species differences, as well as myelinating the axonal arbors, scaling ion channel kinetics to 37° C using a Q_{10} of 2.3, and assigning ion channel properties to the entire axon arbor. The final set of cell types included the layer 1 (L1) neurogliaform cell with a dense axonal arbor (NGC), L2/3 pyramidal cell (L2/3 PC), L4 large basket cell (L4 LBC), L5 thick-tufted pyramidal cell with an early bifurcating apical tuft (L5 PC), and L6 tufted pyramidal cell with its dendritic tuft terminating in L4 (L6 PC). The pyramidal cell

types were selected based on their hypothesized involvement in TMS-evoked corticospinal volleys (I-waves) [31], and the L1 NGC cell type was selected based on its hypothesized involvement in TMS-induced inhibition [32]. Since myelin is expected to reduce thresholds [29], the LBC cell type was selected based on the finding that the vast majority of myelinated, inhibitory axons belong to basket cells [33]. Further details can be found in our previous publication [29] and these models can be downloaded from ModelDB (Model 241165) [34].

We made an additional modification to the L5 and L6 PC models to account for the truncation of their main axons in the slicing process. The main axons of L5 and L6 PCs project subcortically in mature animals, while their collaterals can extend both locally and for several millimeters horizontally [35]. The truncated main axon terminals in these model neurons were therefore unrealistically close to their cell bodies. To exclude them from activation, we disabled these main axon terminals by setting the terminal compartment diameter to 1000 μm. We quantified the effect of disabling the main axon terminals of the L5 and L6 PCs: leaving the main axons intact decreased the thresholds for downward E-fields for at least three of the five L5 PCs and reduced activation of horizontal collaterals (Supplementary Figure 1). Similar effects were observed with the L6 PCs (Supplementary Figure 2). We also generated a simplified version of the L2/3 PC model neurons in which the morphologically-realistic axon was replaced with a straight myelinated axon, similar to previous studies [24]. This straight axon was oriented downward, parallel to the somatodendritic axis and perpendicular to the pial surface. As in the original models, the axon initial segment was modeled as two 30 μm axonal sections, with the diameter drawn from the original reconstructed morphology. The initial segment was connected to alternating sections of myelin and nodes of Ranvier to produce a total length of 1 mm, terminating approximately in L5/6. Matching the myelinated axon models [29], the nodal lengths were 1 μm and the internodal lengths were 100 times the myelin diameter. The nodal diameter was the same as that of the initial segment, and the myelin diameter was set using the diameter-specific ratio of myelin diameter to nodal diameter measured experimentally [33]. Finally, the initial segment, nodes, and internodes were assigned the same membrane properties as those of the morphologically-realistic axon models.

Head model for electric field simulation

Induced E-fields were computed in the realistic volume conductor head model (Figure 2A) provided as default in SimNIBS v2.0, an open-source simulation package that integrates segmentation of MRI scans, mesh generation, and FEM E-field computations [36]. The FEM model was generated using the T1- and T2-weighted images and segmentation from the SimNIBS example data set of a healthy subject, which included white matter, gray matter, cerebrospinal fluid, bone, and scalp tissue volumes. The MRI data were acquired from a healthy subject with the approval of the Ethics Committee of the Medical Faculty of the University of Tübingen [37]. The white matter layer was assigned anisotropic conductivity using the diffusion tensor imaging (DTI) data and the volume normalized approach, with the mean conductivity of each tensor scaled to match the isotropic conductivity of 0.126 S/m [38]. The remaining four tissue volumes were assigned isotropic conductivities [7] (in S/m): gray matter: 0.276, cerebrospinal fluid: 1.790, bone: 0.010,

scalp: 0.250. The final mesh comprised approximately 200,000 nodes and 3.6 million tetrahedral elements. (See [37] for further modeling details). E-field distributions were computed with the SimNIBS models of the MagVenture MC-B70 figure-of-8 coil (P/N 9016E056, MagVenture A/S, Farum, Denmark), which has ten windings with outer and inner diameters of 10.8 and 2.4 cm, respectively [39], or the Magstim 70 mm figure-of-8 coil (P/N 9925–00, Magstim Co., Spring Gardens, Whitland, Carmarthenshire, UK), which has nine windings with outer and inner diameters of 8.8 and 5.2 cm, respectively [40], both for a coil-to-scalp distance of 2 mm and a coil current of 1 A/μs. The MagVenture coil was used for simulations with conventional TMS waveforms to match the experimental setup of [41], and the Magstim coil was used for simulations with cTMS1 waveforms to match the setup of [14]. We simulated TMS of the left hand motor area by positioning the coil over the motor hand knob, located on the precentral gyrus [42]. Following the convention for TMS of M1, the coil was oriented to induce currents perpendicular to the central sulcus, directed 45° relative to the midline (Figure 2A); for monophasic posterior–anterior (P–A) stimulation, this orientation corresponds to the lowest threshold for evoking motor activity, measured by motor evoked potentials (MEPs) in the first dorsal interosseous or abductor digiti minimi, although there is considerable inter-individual variability [43,44].

Embedding neurons in head model

To generate layer-specific populations of neurons, surface meshes representing the cortical layers were interpolated between the gray and white matter surface meshes at normalized depths (the total depth of gray matter is 1): L1: 0.06, L2/3: 0.4, L4: 0.55, L5: 0.65, L6: 0.85 (Figure 2C). These depths were estimated from primate motor cortex slices, in which the boundaries between adjacent layers were at normalized depths of 0.08 (L1–L2/3), 0.51 (L2/3–L4), 0.59 (L4–L5), and 0.81(L5–L6) [45]. M1 is traditionally thought to lack a layer 4 [46], but it was included here based on studies in both mice and primates that demonstrated a functional layer 4 in motor cortex with canonical inputs from thalamus and intra-columnar outputs to L2/3 [47–49].

A $32 \times 34 \times 50$ mm^3 region of interest (ROI) containing the M1 hand knob on the pre-central gyrus and the portion of the postcentral gyrus opposite to it was selected for populating with model neurons (shown in red in Figure 2A). Layer surface meshes were discretized with 3000 triangular elements per surface, yielding a density of approximately 1.7 elements per mm^2. Single model neurons were placed in each of the 3000 elements by centering the cell bodies within the elements (Figure 2B). Based on typical columnar structure [50,51], the model neurons were oriented to align their somatodendritic axes with the element normals and randomly rotated about their somatodendritic axes in the azimuthal direction (see Figure 1A for definition of spherical coordinates). Each model neuron was simulated for five additional azimuthal rotations in 60° increments to sample the full range of possible orientations, and the five clones of each cell type were co-located within each element, increasing the effective cell density thirty-fold to approximately 50.7 cells/mm^2 in each layer. Figure 2D depicts, in a cross-section of the hand knob, the placement of a single clone of each cell type in all five layers as well as the L2/3 and L5 PC populations plotted alone with different colors assigned to axons, apical dendrites, and basal dendrites. Mesh generation, placement of neuronal morphologies, extraction of E-field vectors from the

SimNIBS output, NEURON simulation control, analysis, and visualization were conducted in MATLAB (R2016a & R2017a, The Mathworks, Inc., Natick, MA, USA).

Coupling electric fields to neuronal simulations

Using the quasi-static approximation [52,53], the TMS induced E-field was separated into its spatial and temporal components. Therefore, the relative spatial distribution of the E-field is independent of frequency and does not change with time during the pulse waveform [54]. For each location, the E-field amplitude was obtained by computing the E-field (in V/m) in SimNIBS for a single coil current frequency—specified with the current rate of change in A/μs—and multiplying it by the desired current rate of change at any point in time. The cable equation has been adapted for magnetically induced E-fields to one-dimensional compartmental models [17,18,55]. The spatial component of the exogenous E-fields can be applied to cable models using NEURON's extracellular mechanism [30], which requires expressing the E-field in terms of an extracellular scalar potential at each compartment. However, magnetic induction produces a non-conservative E-field distribution that cannot be converted to scalar potentials. To couple the E-fields computed in the FEM simulations of TMS to the cable models, *quasipotentials* [18,20] were calculated for each cell by numerically integrating the E-field component along each neural process

$$\psi_c = \psi_p - \int \vec{E} \cdot d\vec{s} \approx \psi_p - \frac{1}{2}\left(\vec{E}_c + \vec{E}_p\right) \cdot \vec{s}_{pc}, \tag{1}$$

Where ψ is the extracellular quasipotential, $\vec{E}$ is the E-field vector, $\vec{s}$ is the displacement vector, and subscripts c and p indicate the current/child compartment and previous/parent compartment in the tree structure with the soma arbitrarily designated as the root and reference point ($\psi_{soma} = 0$). The E-field at the model neuron compartments ($\vec{E}_{c,p}$) was linearly interpolated from the 10 nearest mesh points (tetrahedral vertices in SimNIBS) within the gray and white matter volumes using the MATLAB scatteredInterpolant function. The quasipotentials were then calculated at the compartment centers, and then directly substituted as extracellular potentials in NEURON.

With the spatial distribution of quasipotentials determined, the temporal component of the E-field was included by uniformly scaling the distribution over time by various current waveforms. Monophasic, half sine, and biphasic waveforms generated by a MagPro X100 stimulator (MagVenture A/S, Denmark) with a MagVenture MCF-B70 figure-of-8 coil (P/N 9016E0564) were recorded using a search coil and sampling rate of 5 MHz (shown in Figure 5 and Figure 7). We also used waveforms generated by a cTMS1 device with a Magstim 70 mm figure-of-8 coil for 30, 60, and 120 μs pulse widths (shown in Figure 8B) [14,56]. The TMS E-field waveforms were down-sampled with 5 μs time steps for computational efficiency, and normalized to unity amplitude for subsequent scaling in the neural simulations.

As in our previous study [29], the neural models were discretized with isopotential compartments no longer than 20 μm and solved using the backward Euler technique with a time step of 5 μs. The membrane potential of each compartment was allowed to equilibrate

to steady state before stimulation was applied. Activation was defined as membrane potential crossing 0 mV with positive slope in at least 3 compartments within the cell, initiating an action potential.

In addition to the TMS-induced E-field distributions, neural simulations were also performed using uniform E-fields and TMS waveforms, following the quasi-uniform field assumption of transcranial stimulation [57]. The extracellular potential V_e at each compartment with position (x, y, z) was calculated with

$$V_e(x, y, z) = -|E| \cdot (x \sin \theta \cos \phi + y \sin \theta \sin \phi + z \cos \theta), \qquad (2)$$

where the direction of the uniform E-field was given by polar angle θ and azimuthal angle ϕ, in spherical coordinates with respect to the somatodendritic axes (Figure 1A–B), and the potential of the origin (soma) was set to zero [29]. We applied the MagProX100 monophasic TMS pulse waveform with a uniform E-field distribution at directions spanning the polar and azimuthal directions in steps of 15° and 10°, respectively, for a total of 398 directions, and we converted the spherical distribution of thresholds into 2D threshold–direction maps using the Mollweide projection (Figure 1C–D). The overall sensitivity of each model neuron to E-field direction was quantified by the *threshold anisotropy*, defined as the ratio of the maximum and minimum thresholds across all E-field directions. Additionally, the sensitivity to specific E-field directions for each model neuron was quantified by taking the average threshold for E-fields directed transverse ($60° < \theta \le 120°$) and approximately parallel to the somato-dendritic axis—either outward, towards the pial surface ($0 \le \theta \le 60°$), or inward, towards the white matter ($120° < \theta \le 180°$)—after averaging thresholds across all azimuthal rotations within the relevant polar angles.

Neural activation thresholds and time constants

For the coupled FEM E-field and cortical layer model, single neuron thresholds were determined by scaling the coil current's rate of change at pulse onset—which was proportional to the stimulator voltage—using a binary search algorithm to determine the minimum intensity necessary to elicit an action potential with 0.05 A/μs accuracy. For the uniform E-field simulations, threshold E-field magnitudes were obtained with 0.05 V/m accuracy.

Experimentally measured motor threshold (MT) quantifies the stimulus intensity that activates a population of corticospinal neurons, indirectly for most TMS coil configurations, with sufficient excitatory input to drive motoneurons innervating the muscle of interest. Since our model lacks intracortical and corticospinal synaptic connections, it cannot directly predict corticospinal activity or muscle excitation. Therefore, we devised an approximate representation of MT for a hand muscle. We identified a putative hand muscle representation that included both the gyral lip and upper sulcal wall (Figure 2A; Figure 7), where corticomotoneuronal projections to the corresponding spinal motoneurons originate [58] and finger-tapping in the first dorsal interosseous muscle evokes functional MRI activation [10]. Within this hand muscle representation, we approximated MT using the threshold to activate a given percentile of model neurons, across all positions, clones, and azimuthal rotations. We then obtained this percentile-defined MT, Θ, for 30, 60, and 120 μs cTMS1 pulses to

estimate the neural time constant using the same parameter estimation method as used in previous studies [14,59]. In this method, the neural membrane was approximated as a low-pass filter with time constant τ_m, yielding the following strength-duration curve:

$$\widehat{\Theta}\left(t_p\right) = \frac{\Theta_{rh}}{r\left(\tau_m, t_p\right)} .$$

(3)

Here, $\widehat{\Theta}\left(t_p\right)$ was the predicted MT for pulse duration t_p, Θ_{rh} was the rheobase, and $r(\tau_m, t_p)$ was the depolarization factor, calculated as the peak of the low-pass filtered TMS waveform. The parameters τ_m and Θ_{rh} were estimated by least-square fitting of the parametric curve $\widehat{\Theta}$ to the MT from the neural simulations, i.e., by minimizing the sum of relative errors squared $(\widehat{\Theta}/\Theta - 1)^2$ across all pulse durations. The number and precise locations of cortical neurons activated at MT is unknown, so we computed time constants using neural population thresholds in the hand muscle representation for a range of percentiles: 2.5, 5, 10, 25, and 50%.

Code and data availability

The code and relevant data of this study are released on GitHub [60].

Results

Threshold and directional sensitivity vary by cell type

We quantified variations in excitation threshold and intrinsic sensitivity to local E-field direction for each model neuron, independent of their cortical location and the E-field non-uniformity in the head model (Figure 1A–D). For all E-field directions, the site of maximal depolarization and action potential initiation was an axonal termination aligned with the E-field. Consequently, the densely-branching axonal arbors exhibited numerous possible activation sites, and the orientations where specific axonal branches aligned with the E-field in each model neuron corresponded to local minima in the threshold–direction maps.

Thresholds varied substantially both within and between cell types. Within cell type, the minimum threshold amplitudes varied by 18%–73% relative to the lowest threshold clone (Figure 1E). Based on the median within each cell type, the minimum threshold amplitudes were lowest for the L5 PC, followed by the L4 LBC, L2/3 PC, L6 PC, and L1 NGC (Figure 1E). Notably, the minimum threshold among the L2/3 PCs was lower than that of the L5 PCs, despite the higher median.

Threshold anisotropies were used to characterize directional sensitivity and were higher for the pyramidal cell types (2.29–5.09) compared to the interneurons (1.73–3.45) (Figure 1D). The higher threshold anisotropies in the pyramidal cells reflected their more asymmetric, elongated axons relative to the more spherically-symmetric axons of the interneurons, which have a broader distribution of axon branch orientations. The mean threshold differences between transverse and inward or outward E-fields, relative to the somatodendritic axis of each model neuron, ranged from −34% to 32% (positive value indicates higher threshold for transverse E-field) (Supplementary Figure 3). L5 PCs had the strongest preference for both

inward and outward E-field directions, relative to transverse, followed by the L2/3 PCs and L4 LBCs, while the L1 NGCs and L6 PCs generally had lower thresholds for transverse E-field directions (Figure 1D; Supplementary Figure 3). When the realistic axon morphologies were replaced with straight axons, the threshold anisotropy of the L2/3 PCs increased significantly, ranging from 43.1–60.9, with highest thresholds for transverse E-field and lowest thresholds for downward E-field, which were perpendicular and parallel, respectively, to the activated axon terminal—the exclusive activation site (Supplementary Figure 4).

In addition to these well-characterized and validated models [29], we also applied the same age- and species-related modifications to the entirety of the model neurons in the Blue Brain library—scaling the original juvenile, rat neuron models to the properties of mature, human cortical neurons—and determined their minimum thresholds for activation with uniform E-fields. The inhibitory basket cell types in L2/3, L5, and L6 had thresholds that were comparable to the L4 LBCs; similarly, the subset of pyramidal cell types we selected were representative of the thresholds of the remaining pyramidal cell types within their respective layers (Supplementary Figure 5). Thus, we proceeded with the originally selected set of model neurons for quantifying the effects of TMS.

TMS activates cortical layers 2–5 in gyral crown

We simulated patterns of neural activation by populating the head model with model neurons in a ROI comprising the left motor hand knob in M1 and positioning the TMS coil in an orientation corresponding to the lowest threshold for evoking motor activity (Figure 2). The E-field distribution in the brain was approximately tangential to the scalp, with the largest amplitudes at gyral surfaces perpendicular to the E-field direction, and decayed rapidly with depth into the sulcus (Figure 3A–B). Monophasic stimulation with dominant E-field induced in the P–A direction generated the lowest thresholds in L5 neurons, followed by L2/3 and L4, L6, and L1 (Figure 3C; Figure 7). The recruitment order matched that of uniform E-field stimulation, with some degree of overlap between L2/3 and L4, and activation also occurred exclusively at the terminals of the axon collaterals (Figure 4). In addition to providing anatomically relevant positions for neuron model placement, the realistic gyral geometry in the FEM was necessary to generate accurate E-field and threshold distributions; we additionally simulated a homogeneous intracranial volume, i.e., using the gray matter conductivity also for the white matter and cerebrospinal fluid volumes, which resulted in weaker and more diffuse E-field distribution [61] and thus higher thresholds and less focal activation (Supplementary Figure 6A–B).

Previous publications hypothesized that the threshold for neural activation by TMS is inversely proportional to either the E-field magnitude [10] or its normal component relative to the cortical surface, based on the orientation of cortical columns [62,63], thereby generating the lowest thresholds in either the gyral crown or the sulcal wall, respectively. Thresholds were lowest in the pre- and postcentral gyral crowns for all five layers, corresponding to regions of maximal E-field amplitude (Figure 3C). The low threshold regions also extended to the gyral fold lateral to the hand knob, where the E-field magnitude remained high relative to the peak under the coil center, as well as deeper into the posterior wall of the central sulcus relative to the anterior wall (Supplementary Figure 7). Thresholds

within the sulcal walls were substantially higher than the more superficial gyral regions, and activation reached relatively deeper into the sulcal wall for the low-threshold middle layers: L2–L5. Throughout the ROI, the thresholds of all cell types were more strongly correlated with the local E-field magnitude (R^2 0.913) than the normal component (inward: R^2 0.528; outward: R^2 0.518) (Figure 3D), indicating that the E-field magnitude was a markedly stronger driver of neuronal activation than the normal component.

Activation depends on stimulus waveform and direction

Shifts in action potential initiation sites with current direction led to layer- and waveform-specific shifts in the spatial distributions of thresholds. For monophasic P–A stimulation, the activated terminals in the low-threshold L2–L5 were located in the downward projecting axonal branches in the gyral lip and sulcal wall and the horizontal and oblique collaterals in the gyral crown (Figure 4). For reversed monophasic stimulation in the anterior–posterior (A–P) direction, activation shifted to an axonal terminal in the opposite direction for each model neuron (Figure 4). These new action potential initiation sites were activated with a higher or lower threshold for each model neuron, and the threshold changes depended on the pulse waveform, cell type, and position in the cortical geometry.

Using the same current direction, monophasic, half sine, and biphasic pulses produced similar threshold distributions, with the lowest thresholds in the gyral crown and lip (Figure 5A–C). Switching from P–A to A–P monophasic TMS resulted in an anterior shift of activation in L2–L5 of the pre-central gyrus; in the analysis plane, thresholds were up to 30% higher on the posterior lip and up to 45% lower on the anterior lip (Figure 5D). In contrast, for the half sine and biphasic waveforms, which have similar peak E-field strengths in each phase, the shifts in activation were in the same direction, but substantially reduced. Note that for biphasic pulses, the second phase with longer duration and direction opposite to the initial phase was the dominant one, and therefore the effect of directionality was reversed [19,41]. The effect of current direction on threshold was similar in L2–5 for the homogeneous intracranial conductivity case but with reduced threshold differences (Supplementary Figure 6C–D). To investigate the effect of the realistic axon morphologies on the spatial distribution of thresholds, we also simulated monophasic P–A and A–P stimulation for the L2/3 PCs with straight axons (Figure 6). P–A TMS activated with lowest intensity L2/3 PCs in the upper portion of the anterior wall of the central sulcus, while A–P TMS activated the opposite sulcal wall, with no low-threshold gyral activation for either direction (Figure 6A–B). While A–P TMS also produced an anterior shift in activation for the straight axon models, thresholds were up to 250% higher on the posterior side of the precentral gyrus and up to 70% lower on the anterior side (Figure 6C). Thus, including realistic PC axon morphologies resulted in superficial, gyral activation that exhibited slight anterior shifts for A–P relative to P–A TMS, whereas approximating the axon as straight and oriented normal to the cortical surface produced more sulcal activation with substantially higher direction dependence, as expected based on uniform E-field simulations (Supplementary Figure 4).

Linear regressions between the median thresholds of the model neurons within the putative hand muscle representation [10] and experimentally measured MTs [41] (Figure 7) across all

waveforms and directions yielded strong correlations in all layers ($R^2 > 0.75$; $p < 0.03$), with the strongest correlations in L2–L5 ($R^2 > 0.85$) (Supplementary Figure 8A). Varying the threshold percentile used for regression led to minimal changes in correlation coefficients in nearly all cases ($R^2 > 0.69$; $p < 0.05$), except the correlations in L1 for 2.5% and 10% threshold percentiles, which fell below statistical significance (Supplementary Figure 8B). When the current direction was reversed from P–A to A–P, the L1 and L6 neurons exhibited less than a 5% change in threshold for all pulse waveforms. In contrast, for the L2–L5 neurons, the threshold increased by 8–33% for all pulse waveforms, with a greater increase for the monophasic pulse than for the half-sine and biphasic pulses, consistent with the experimental data [41] (Figure 7). These effects were consistent across sub-regions of the putative hand muscle representation (Supplementary Figure 9).

Model strength–duration time constants match experiments

Time constants of single model neurons exhibited slight variations throughout the ROI for the L4 LBCs and L5 PCs, while the L2/3 PCs had consistently longer time constants in the posterior-facing sulcal walls throughout the ROI (Figure 8A). Using median thresholds in the putative hand muscle representation, the strength–duration curves for L2–L5 neurons agreed remarkably well with experimental measurements (Figure 8B). The proportion of activated cortical neurons corresponding to MT is unknown, but the slight variation of time constant showed insensitivity to the proportion of activation and overall agreement with the experimental estimate (200 ± 33 μs; mean ± SD) [14] (Figure 8C). L2/3 PCs had longer time constants (288 – 333 μs) than model neurons in the other layers and the experimental estimate, and this was consistent with the markedly increased time constants in the sulcal wall as estimated using single neuron thresholds (Figure 8A).

Discussion

We developed a detailed, multi-scale model of the direct cortical response to TMS by populating an MRI-derived FEM head model with realistic models of neurons across the cortical layers. The neuron models approximated the geometry of human cortical cells and included extensive axonal arbors, which were necessary to predict the dependence of activation on stimulation direction in each cell type. The results revealed several important conclusions regarding the neural mechanisms of TMS of the motor cortex. TMS exclusively activated neurons at their axon terminals aligned to the local E-field direction. Due to their complex axonal morphology, neurons were activated by E-fields both normal and tangential to the cortical surface, and the E-field magnitude was a much stronger predictor of neural activation than the E-field component normal to the cortical surface. In both the uniform E-field threshold–direction maps and the multi-scale model, thresholds varied substantially across neurons in different cortical layers, in a manner that did not simply reflect their respective distances from the coil: the L5 PCs had the lowest thresholds, followed by L2/3 PCs, L4 LBCs, L6 PCs, and L1 NGCs. There was substantial overlap in the threshold distributions of the neurons in L2–5, resulting in mixed cell-type recruitment at suprathreshold stimulation intensities, whereas L1 and L6 neurons were hardly activated. TMS of M1 activated with lowest intensity neurons in the crown and lip of the precentral gyrus due to the higher E-field magnitude there as compared to the sulcal wall. Reversing

the current direction from P–A to A–P caused an anterior shift in the threshold distributions of L2/3–L5, with the strongest effects in the pyramidal cell types and for the monophasic waveform. These trends agreed remarkably well with variations in MT observed in human subjects.

TMS preferentially activated axon terminals in all cell types, in both the uniform and non-uniform E-fields. As such, our results differ from two widely cited modeling studies which concluded that TMS initiates action potentials at the soma or initial segment [23,24]. Indeed, their results can be explained by implementation errors in the equivalent current injection method representing the coupling between the E-field and the neural cable models, in which the current applied to the neural compartments had a dimensional mismatch and was unbalanced at the termination, connection, and branching points of the neural cable [18,64–66]. Consequently, Seo et al. [24] reported TMS activation with higher thresholds for larger diameter L5 PCs compared to smaller diameter L3 PCs, which did not follow the reversed recruitment order of extracellular stimulation [67–69]; the threshold distribution maps were also highly fragmented, which is implausible given the continuous distribution of the macroscopic FEM E-field and quasi-uniformity of E-field on microscopic scales in transcranial brain stimulation [57]. Activation at the soma or dendrites is also unlikely due to their long membrane time constants (> 5 ms) compared to myelinated axons (< 400 μs) [70,71]. These axonal time constants agree with strength–duration time constants measured for TMS of the motor cortex [14,59], and were reproduced by our models. In contrast, direct polarization of cell bodies (2–3 mV), before an axonal compartment was activated by suprathreshold TMS pulses, was well below action potential threshold. Further evidence for preferential activation of axonal terminals comes from experimental data on the corticospinal I_1-wave [72], which is thought to originate from excitatory, monosynaptic inputs to the pyramidal tract neurons projecting directly to hand motoneurons [31]. The I_1-wave threshold is relatively unaffected by voluntary contraction, GABAergic drugs, or the paired-pulse paradigm known as short-interval intracortical inhibition [72]. This is expected if the pre-synaptic inputs to PTNs were activated at their distal axon terminals, where the membrane potential is less affected by synaptic inputs than the dendrites, soma, or axon initial segment. Thus, our finding that TMS preferentially activated axon terminals, while inconsistent with some prior modeling studies, is consistent with experimental results.

Including realistic axonal geometries is critical to predicting accurately the variations in threshold and directional sensitivity within and between cell types, and this had significant implications for the mechanisms of neural activation in the full model. Previous biophysical models and our simulations with idealized, straight axons found extremely high threshold anisotropies and could not predict variations in collateral activation across cell types [19,24]. In particular, inhibitory interneurons possess highly branched axons that cannot be approximated unambiguously with a single axon direction. On the other hand, we observed significant variations in activation thresholds both between and within cell types as a result of axonal geometry. In addition, the phenomenological cortical column cosine model argues that pyramidal cells are depolarized by E-field directed into the cortical surface (parallel to the cortical columns), while interneurons are depolarized by tangential fields [62,63,73]. This led to the prediction that TMS activates pyramidal cells in the sulcal wall, where the E-field is directed into the cortical surface, and therefore, neural activation should be

proportional to the normal component of the E-field [62,63,73]. Our simulations of L2/3 PCs with straight axons largely follow the predictions of this phenomenological theory, as thresholds were lowest in the gyral lip and superficial sulcal wall and highest in the gyral crown. In contrast, while the low-threshold cells in our model (L2–5) exhibited a preference for normal relative to transverse E-field, this effect was relatively small, with typical threshold differences of less than 30% (Supplementary Figure 3). Since the E-field activated the terminals of aligned axonal branches, but not cell bodies or dendrites, the dense axon collateralization of cortical PCs and interneurons enabled activation for all E-field directions [29]. Consequently, the spatial distribution of thresholds for a given coil configuration was much more highly correlated with the E-field magnitude than its normal component. Neural activation is therefore more likely to occur in the gyral crown and lip, which are exposed to larger E-field magnitudes, than the sulcal wall. These results provide a clear mechanistic explanation of recent studies relating MTs for a range of TMS coil orientations and positions with E-field distributions calculated in subject-specific head models [9,10,74].

The integrated model enabled analysis of waveform- and direction-dependent effects that would be indiscernible using the E-field distribution alone. TMS of the motor cortex produces MEPs with 2–3 ms longer latencies for current in the A–P than in the P–A direction [11,41,59,75,76]. In the model, reversing the current direction for the monophasic waveform from P–A to A–P produced an anterior shift in the spatial distribution of activation of L2/3 and L5 PCs. These shifts with current direction were explained by the uniform E-field threshold–direction maps for these cell types, as they indicated slight preferences for E-fields oriented into the cortical surface for L2–5 neurons (Supplementary Figure 3). While this preference was insufficient to reduce thresholds in the sulcal wall, where the E-field is nearly perpendicular to the cortical surface, it did alter thresholds within the precentral gyrus dependent on the current direction. This waveform-dependent shift in the region of cortical activation could explain the longer MEP latencies of monophasic A-P stimulation relative to P-A stimulation, which is not observed for the more symmetric waveforms. Corticomotoneuronal cells that make monosynaptic connections with alpha motoneurons are found mostly in the anterior bank of the central sulcus [58]. Based on our model, P–A stimulation would therefore mostly activate the corticomotoneuronal cells monosynaptically, producing MEPs with shorter latencies, while A–P stimulation would activate rostral M1 or pre-motor pyramidal cells producing MEPs polysynaptically with longer latencies. In fact, excitatory inputs to M1 from ventral and dorsal pre-motor cortex were identified in monkeys [77–79] and humans [80] with conduction latencies matching late I-waves generated by single-pulse TMS [81], suggesting they may be recruited by A–P stimulation [72]. These results support that A–P and P–A stimulation of M1 activate different sets of cortical neurons that indirectly generate downstream corticospinal activity, rather than different sites within the same neurons, as argued elsewhere [72].

Experimentally validating these predictions in humans may be difficult with current experimental techniques, but invasive recordings in non-human primates provide access to cortical activity during TMS that could measure the cell-type- and location-specific responses to TMS [3]. Still, one strategy to permit more direct comparisons between the model and human experiments is to simulate evoked responses measurable by less invasive methods, including at the corticospinal and muscle levels as well as at the scalp.

Although a substantial advance over prior work, several limitations of the model should be noted. Obtaining realistic threshold amplitudes in neural models of TMS is a persistent challenge for the field [19–21]. Sommer et al. reported MTs for monophasic P–A stimulation between 45.6–102.6 A/μs for subjects at rest [41]. These values are close to the minimum threshold of L5 PCs in the putative hand muscle representation within our model (68.7 A/μs); however, sub-MT stimuli are known to activate intracortical circuits [82], suggesting that model thresholds may still be too high. Our results showed heterogeneous tissue conductivities in the FEM model were important to obtain more accurate E-field distribution and lower thresholds. Uniform overestimation of the activation thresholds may be related to limitations in the axon models, specifically in the sodium channel model, as well as differences in morphological features related to age, species, and brain region [29]. Additionally, we simulated quiescent cells in this study, but endogenous sub- or supra-threshold synaptic activity may reduce thresholds in both directly and indirectly activated neurons; subthreshold somatic depolarization (hyperpolarization) can reduce (increase) thresholds via passive axonal polarization (Supplementary Figure 10).

Another limitation was the lack of corticospinal models extending into the white matter, which may be activated directly by TMS with certain coil configurations [72], as well as medium to long-range intracortical axonal inputs. These range from intrinsic horizontal connections between different cortical columns within several millimeters [49,83,84], association fibers that connect ipsilateral cortical regions via white matter, such as the U-fiber system [85], and subcortical or callosal projections through long-range white matter tracts [86]. Our model included local axon collaterals forming the local columnar connections within a few hundred microns [87]. TMS-fMRI studies have shown, for example, that short stimulation trains applied to premotor cortex modulate activity in a number of distant connected regions, including contralateral primary and secondary motor areas [88,89]. Additionally, dual-coil TMS paradigms, in which a test pulse is applied to M1 to evoke an MEP following a conditioning pulse applied to a distant region (e.g. contralateral M1 or cerebellum), show that activation of these long range connections can modulate motor output [90–92]. Incorporating these additional axonal projections may be necessary to make stronger conclusions about which neural elements TMS activates and the indirect effects on their post-synaptic targets. In particular, our model predicted inhibitory interneurons have similar or higher thresholds for direct activation relative to the model pyramidal cells, mainly due to their smaller axonal diameters. This implies that inhibitory effects of sub-MT intensity TMS [93,94] are mediated by low-threshold excitatory inputs to these inhibitory interneurons. This would agree with the model of indirect inhibitory activation proposed by Bestmann et al. based on their findings using a triple pulse TMS paradigm of M1 [95]: two subthreshold conditioning stimuli facilitated inhibition of the motor output evoked by a suprathreshold test stimulus, suggesting the conditioning stimuli activated convergent excitatory inputs of a population of inhibitory interneurons in which temporal summation occurred. These excitatory inputs could either be the local axons we modeled, or intrinsic/extrinsic inputs we did not model, as discussed above. Inhibitory interneurons have lower thresholds for indirect, synaptic activation due to their higher input resistance (lower somatic surface area), which would explain how activation of low threshold excitatory elements could lead to a dominant inhibitory effect at certain stimulus

intensities. The trajectories of corticofugal projections can be incorporated using DTI tractography [38,96], whereas obtaining intracortical projections is more challenging. Also, we focused on modeling a single excitatory or inhibitory cell type per layer, but there were additional cortical cell types with low thresholds for activation that we did not simulate in the full multi-scale model. Our supplementary simulations suggest inhibitory basket cells in L2/3, L5, and L6 may be recruited by TMS at similar amplitudes to the L4 large basket cells.

We also focused on direct activation by TMS and did not include synaptic connections between neurons. Previous simulation studies used network models with simplified representations of neurons to reproduce several characteristics of the corticospinal activity evoked by TMS [97,98], but they did not explicitly model the interaction between the induced E-field and the neural elements. Instead, to represent the stimulus, the models relied on the authors' own assumptions regarding the number, location, and connectivity of directly activated neurons, essentially using random activation of a selected proportion of cells or synapses. By including the biophysical mechanisms involved in the interaction between the spatial and temporal features of the E-field and the cortical circuits, our modeling framework captures the shortest-latency response of the cortical circuits to a TMS pulse and can feed into higher-level network models. This is a required first step for constructing more complex models that include synaptic connectivity and characterizing the subsequent indirect effects of activation, which is especially important to strengthen conclusions about the role of direct and indirect inhibitory activation discussed earlier. Network models with both reconstructed morphologies and realistic simulations of the E-field pose a computational challenge, but may be important in modeling short-term circuit dynamics in response to TMS.

Finally, methods for computing the TMS-induced E-field in FEM models have limitations, including the assumption of homogeneous, isotropic conductivities in gray matter and the sharp conductivity boundary at its border with the white matter [36]. In our model, the unnatural E-field gradients did not produce activation in L5/6 PC axons that crossed the gray–white matter boundary, suggesting the latter issue is not critical. Additionally, we used a single subject's head model, and sites of activation may vary with cortical geometry [99].

In conclusion, this work introduces a computational modeling platform for simulating the response of cortical neurons to transcranial magnetic stimulation and enables quantification of the effects of pulse waveforms, coil configurations, and individual head anatomies on the cell type specific cortical response. Our results demonstrate the importance of incorporating non-linear neural membrane dynamics and realistic axon morphologies to capture the effect of the stimulation parameters. This platform will allow continued mechanistic studies and optimization of TMS and other cortical stimulation technologies to guide the rational design of non-invasive brain therapies.

Supplementary Material

Refer to Web version on PubMed Central for supplementary material.

Acknowledgments

References

[1]. Barker AT, Jalinous R, Freeston IL. Non-invasive magnetic stimulation of human motor cortex. Lancet 1985;1:1106–7. doi:10.1016/S0140-6736(85)92413-4. [PubMed: 2860322]

[2]. Lefaucheur JP, Andre-Obadia N, Antal A, Ayache SS, Baeken C, Benninger DH, et al. Evidence-based guidelines on the therapeutic use of repetitive transcranial magnetic stimulation (rTMS). Clin Neurophysiol 2014;125:2150–206. [PubMed: 25034472]

[3]. Mueller JK, Grigsby EM, Prevosto V, Petraglia FW, Rao H, Deng Z-D, et al. Simultaneous transcranial magnetic stimulation and single-neuron recording in alert non-human primates. Nat Neurosci 2014;17:1130–6. doi:10.1038/nn.3751. [PubMed: 24974797]

[4]. Li B, Virtanen JP, Oeltermann A, Schwarz C, Giese MA, Ziemann U, et al. Lifting the veil on the dynamics of neuronal activities evoked by transcranial magnetic stimulation. Elife 2017;6:e30552. doi:10.7554/eLife.30552. [PubMed: 29165241]

[5]. Romero MC, Davare M, Armendariz M, Janssen P. Neural basis of Transcranial Magnetic Stimulation at the single-cell Level. BioRxiv 2018:405753. doi:10.1101/405753.

[6]. Murphy SC, Palmer LM, Nyffeler T, Müri RM, Larkum ME. Transcranial magnetic stimulation (TMS) inhibits cortical dendrites. Elife 2016;5:1–12. doi:10.7554/eLife.13598.

[7]. Chen T-W, Wardill TJ, Sun Y, Pulver SR, Renninger SL, Baohan A, et al. Ultrasensitive fluorescent proteins for imaging neuronal activity. Nature 2013;499:295. [PubMed: 23868258]

[8]. Murthy VN, Sejnowski TJ, Stevens CF. Dynamics of dendritic calcium transients evoked by quantal release at excitatory hippocampal synapses. Proc Natl Acad Sci U S A 2000;97:901–6. doi:10.1073/pnas.97.2.901. [PubMed: 10639177]

[9]. Laakso I, Murakami T, Hirata A, Ugawa Y. Where and what TMS activates: Experiments and modeling. Brain Stimul 2018;11:166–74. doi:10.1016/j.brs.2017.09.011. [PubMed: 29030110]

[10]. Bungert A, Antunes A, Espenhahn S, Thielscher A. Where does TMS stimulate the motor cortex? Combining electrophysiological measurements and realistic field estimates to reveal the affected cortex position. Cereb Cortex 2016;27:5083–94. doi:10.1093/cercor/bhw292.

[11]. Sommer M, Ciocca M, Chieffo R, Hammond P, Neef A, Paulus W, et al. TMS of primary motor cortex with a biphasic pulse activates two independent sets of excitable neurones. Brain Stimul 2018;11:558–65. doi:10.1016/j.brs.2018.01.001. [PubMed: 29352669]

[12]. Casula EP, Rocchi L, Hannah R, Rothwell JC. Effects of pulse width, waveform and current direction in the cortex: A combined cTMS-EEG study. Brain Stimul 2018:1–8. doi:10.1016/j.brs.2018.04.015.

[13]. Hannah R, Rothwell JC. Pulse Duration as Well as Current Direction Determines the Specificity of Transcranial Magnetic Stimulation of Motor Cortex during Contraction. Brain Stimul 2017;10:106–15. doi:10.1016/j.brs.2016.09.008. [PubMed: 28029595]

[14]. Peterchev AV, Goetz SM, Westin GG, Luber B, Lisanby SH. Pulse width dependence of motor threshold and input-output curve characterized with controllable pulse parameter transcranial magnetic stimulation. Clin Neurophysiol 2013;124:1364–72. doi:10.1016/j.clinph.2013.01.011. [PubMed: 23434439]

[15]. Goetz SM, Luber B, Lisanby SH, Murphy DL, Kozyrkov IC, Grill WM, et al. Enhancement of Neuromodulation with Novel Pulse Shapes Generated by Controllable Pulse Parameter Transcranial Magnetic Stimulation. Brain Stimul 2015;9:39–47. doi:10.1016/j.brs.2015.08.013. [PubMed: 26460199]

[16]. Basser PJ, Roth BJ. Stimulation of a myelinated nerve axon by electromagnetic induction. Med Biol Eng Comput 1991;29. doi:10.1007/BF02446708.

[17]. Nagarajan SS, Durand DM. A generalized cable equation for magnetic stimulation of axons. IEEE Trans Biomed Eng 1996;43:304–12. doi:10.1109/10.486288. [PubMed: 8682543]

[18]. Wang B, Grill WM, Peterchev AV. Coupling Magnetically Induced Electric Fields to Neurons: Longitudinal and Transverse Activation. Biophys J 2018;115:95–107. doi:10.1016/j.bpj. 2018.06.004. [PubMed: 29972816]

[19]. Salvador R, Silva S, Basser PJ, Miranda PC. Determining which mechanisms lead to activation in the motor cortex: A modeling study of transcranial magnetic stimulation using realistic stimulus waveforms and sulcal geometry. Clin Neurophysiol 2011;122:748–58. doi:10.1016/j.clinph. 2010.09.022. [PubMed: 21035390]

[20]. Goodwin BD, Butson CR. Subject-Specific Multiscale Modeling to Investigate Effects of Transcranial Magnetic Stimulation. Neuromodulation 2015;18:694–704. doi:10.1111/ner.12296. [PubMed: 25953411]

[21]. Wu T, Fan J, Lee KS, Li X. Cortical Neuron Activation Induced by Electromagnetic Stimulation: A Quantitative Analysis via Modeling and Simulation. J Comput Neurosci 2016:3–5. doi: 10.1007/s10827-015-0585-1.

[22]. Kamitani Y, Bhalodia VM, Kubota Y, Shimojo S. A model of magnetic stimulation of neocortical neurons. Neurocomputing 2001;38:697–703. doi:10.1016/S0925-2312(01)00447-7.

[23]. Pashut T, Wolfus S, Friedman A, Lavidor M, Bar-Gad I, Yeshurun Y, et al. Mechanisms of magnetic stimulation of central nervous system neurons. PLoS Comput Biol 2011;7. doi:10.1371/journal.pcbi.1002022.

[24]. Seo H, Schaworonkow N, Jun SC, Triesch J. A multi-scale computational model of the effects of TMS on motor cortex. F1000Research 2017:1–12. doi:10.12688/f1000research.9277.1.

[25]. Wagner T, Eden U, Rushmore J, Russo CJ, Dipietro L, Fregni F, et al. Impact of brain tissue filtering on neurostimulation fields: A modeling study. Neuroimage 2014;85:1048–57. doi: 10.1016/j.neuroimage.2013.06.079. [PubMed: 23850466]

[26]. Seo H, Jun SC. Relation between the electric field and activation of cortical neurons in transcranial electrical stimulation. Brain Stimul 2019;12:275–89. doi:10.1016/j.brs.2018.11.004. [PubMed: 30449635]

[27]. Markram H, Muller E, Ramaswamy S, Reimann MW, Abdellah M, Sanchez CA, et al. Reconstruction and Simulation of Neocortical Microcircuitry. Cell 2015;163:456–92. doi: 10.1016/j.cell.2015.09.029. [PubMed: 26451489]

[28]. Ramaswamy S, Courcol J-D, Abdellah M, Adaszewski SR, Antille N, Arsever S, et al. The neocortical microcircuit collaboration portal: a resource for rat somatosensory cortex. Front Neural Circuits 2015;9:1–14. doi:10.3389/fncir.2015.00044. [PubMed: 25713515]

[29]. Aberra AS, Peterchev AV., Grill WM. Biophysically Realistic Neuron Models for Simulation of Cortical Stimulation. J Neural Eng 2018;15:066023. [PubMed: 30127100]

[30]. Hines ML, Carnevale NT. The NEURON simulation environment. Neural Comput 1997;9:1179–209. doi:10.1162/neco.1997.9.6.1179. [PubMed: 9248061]

[31]. Di Lazzaro V, Profice P, Ranieri F, Capone F, Dileone M, Oliviero A, et al. I-wave origin and modulation. Brain Stimul 2012;5:512–25. doi:10.1016/j.brs.2011.07.008. [PubMed: 21962980]

[32]. Di Lazzaro V, Rothwell J, Capogna M. Noninvasive Stimulation of the Human Brain: Activation of Multiple Cortical Circuits. Neurosci 2017;24:246–60. doi:10.1177/1073858417717660.

[33]. Micheva KD, Wolman D, Mensh BD, Pax E, Buchanan J, Smith SJ, et al. A large fraction of neocortical myelin ensheathes axons of local inhibitory neurons. Elife 2016;5:1–29. doi:10.7554/eLife.15784.

[34]. Aberra AS, Peterchev AV., Grill WM. Biophysically realistic neuron models for simulation of cortical stimulation. ModelDB 2018 https://senselab.med.yale.edu/ModelDB/showmodel.cshtml?model=241165 (accessed May 27, 2019).

[35]. Harris KD, Shepherd GMG. The neocortical circuit : themes and variations. Nat Neurosci 2015;18. doi:10.1038/nn.3917.

[36]. Thielscher A, Antunes A, Saturnino GB. Field modeling for transcranial magnetic stimulation: A useful tool to understand the physiological effects of TMS? Proc Annu Int Conf IEEE Eng Med Biol Soc EMBS 2015:222–5. doi:10.1109/EMBC.2015.7318340.

[37]. Windhoff M, Opitz A, Thielscher A. Electric field calculations in brain stimulation based on finite elements: An optimized processing pipeline for the generation and usage of accurate individual head models. Hum Brain Mapp 2013;34:923–35. doi:10.1002/hbm.21479. [PubMed: 22109746]

[38]. Opitz A, Windhoff M, Heidemann RM, Turner R, Thielscher A. How the brain tissue shapes the electric field induced by transcranial magnetic stimulation. Neuroimage 2011;58:849–59. doi:10.1016/j.neuroimage.2011.06.069. [PubMed: 21749927]

[39]. Thielscher A, Kammer T. Electric field properties of two commercial figure-8 coils in TMS: Calculation of focality and efficiency. Clin Neurophysiol 2004;115:1697–708. doi:10.1016/j.clinph.2004.02.019. [PubMed: 15203072]

[40]. Thielscher A, Kammer T. Linking physics with physiology in TMS: a sphere field model to determine the cortical stimulation site in TMS. Neuroimage 2002;17:1117–30. doi:10.1006/nimg.2002.1282. [PubMed: 12414254]

[41]. Sommer M, Alfaro A, Rummel M, Speck S, Lang N, Tings T, et al. Half sine, monophasic and biphasic transcranial magnetic stimulation of the human motor cortex. Clin Neurophysiol 2006;117:838–44. doi:10.1016/j.clinph.2005.10.029. [PubMed: 16495145]

[42]. Yousry TA, Schmid UD, Alkadhi H, Schmidt D, Peraud A, Buettner A, et al. Localization of the motor hand area to a knob on the precentral gyrus. A new landmark. Brain 1997;120:141–57. doi:10.1093/brain/120.1.141. [PubMed: 9055804]

[43]. Kammer T, Beck S, Thielscher A, Laubis-Hermann U, Topka H. Motor threshold in humans: a transcranial magnetic stimulation study comparing different pulse waveforms, current directions and stimulator types. Clin Neurophysiol 2001;112:250–8. doi:10.1016/S1388-2457(00)00513-7. [PubMed: 11165526]

[44]. Balslev D, Braet W, McAllister C, Miall RC. Inter-individual variability in optimal current direction for transcranial magnetic stimulation of the motor cortex. J Neurosci Methods 2007;162:309–13. doi:10.1016/j.jneumeth.2007.01.021. [PubMed: 17353054]

[45]. García-Cabezas MÁ, Barbas H. Area 4 has layer IV in adult primates. Eur J Neurosci 2014;39:1824–34. doi:10.1111/ejn.12585. [PubMed: 24735460]

[46]. Amaral DG. The anatomical organization of the central nervous system In: Kandel ER, Schwarz JR, Jessel TM, editors. Princ. Neural Sci, New York: McGraw-Hill; 2000, p. 317–36.

[47]. Yamawaki N, Borges K, Suter BA, Harris KD, Shepherd GMG. A genuine layer 4 in motor cortex with prototypical synaptic circuit connectivity. Elife 2014;3:e05422. doi:10.7554/eLife.05422. [PubMed: 25525751]

[48]. Barbas H, García-Cabezas MÁ. Motor cortex layer 4: Less is more. Trends Neurosci 2015;38:259–61. doi:10.1016/j.tins.2015.03.005. [PubMed: 25868984]

[49]. Gatter KC, Powell TPS. The Intrinsic Connections of the Cortex of Area 4 of the Monkey. Brain 1978:513–41. [PubMed: 101281]

[50]. DeFelipe J, Alonso-Nanclares L, Arellano JI. Microstructure of the neocortex: Comparative aspects. J Neurocytol 2002;31:299–316. [PubMed: 12815249]

[51]. DeFelipe J, Hendry SHC, Hashikawa T, Molinari M, Jones EG. A microcolumnar structure of monkey cerebral cortex revealed by immunocytochemical studies of double bouquet cell axons. Neuroscience 1990;37:655–73. doi:10.1016/0306-4522(90)90097-N. [PubMed: 1701039]

[52]. Plonsey R, Heppner DB. Considerations of quasi-stationarity in electrophysiological systems. Bull Math Biophys 1967;29:657–64. doi:10.1007/BF02476917. [PubMed: 5582145]

[53]. Bossetti CA, Birdno MJ, Grill WM. Analysis of the quasi-static approximation for calculating potentials generated by neural stimulation. J Neural Eng 2008;5:44–53. doi: 10.1088/1741-2560/5/1/005. [PubMed: 18310810]

[54]. Wang W, Eisenberg SR. A three-dimensional finite element method for computing magnetically induced currents in tissues. IEEE Trans Magn 1994;30. doi:10.1109/20.334289.

[55]. Roth BJ, Basser PJ. A Model of the Stimulation of a Nerve Fiber by Electromagnetic Induction. IEEE Trans Biomed Eng 1990;37:588–97. doi:10.1038/165089b0. [PubMed: 2354840]

[56]. Peterchev AV, Jalinous R, Lisanby SH. A transcranial magnetic stimulator inducing near-rectangular pulses with controllable pulse width (cTMS). IEEE Trans Biomed Eng 2008;55:257–66. doi:10.1109/TBME.2007.900540. [PubMed: 18232369]

[57]. Bikson M, Dmochowski JP, Rahman A. The "quasi-uniform" assumption in animal and computational models of non-invasive electrical stimulation. Brain Stimul 2013;6:704–5. doi: 10.1016/j.brs.2012.11.005. [PubMed: 23290681]

[58]. Rathelot J-A, Strick PL. Subdivisions of primary motor cortex based on cortico-motoneuronal cells. Proc Natl Acad Sci U S A 2009;106:918–23. doi:10.1073/pnas.0808362106. [PubMed: 19139417]

[59]. D'Ostilio K, Goetz SM, Hannah R, Ciocca M, Chieffo R, Chen J-CA, et al. Effect of coil orientation on strength–duration time constant and I-wave activation with controllable pulse parameter transcranial magnetic stimulation. Clin Neurophysiol 2016;127:675–83. doi:10.1016/j.clinph.2015.05.017. [PubMed: 26077634]

[60]. Aberra AS. TMSsim_Aberra2019. GitHub 2019. doi:10.5281/zenodo.2488572.

[61]. Thielscher A, Opitz A, Windhoff M. Impact of the gyral geometry on the electric field induced by transcranial magnetic stimulation. Neuroimage 2011;54:234–43. doi:10.1016/j.neuroimage. 2010.07.061. [PubMed: 20682353]

[62]. Fox PT, Narayana S, Tandon N, Sandoval H, Fox SP, Kochunov P, et al. Column-Based Model of Electric Field Excitation of Cerebral Cortex. Hum Brain Mapp 2004;22:1–14. doi:10.1002/hbm. 20006. [PubMed: 15083522]

[63]. Krieg TD, Salinas FS, Narayana S, Fox PT, Mogul DJ. PET-based confirmation of orientation sensitivity of TMS-induced cortical activation in humans. Brain Stimul 2013;6:898–904. doi: 10.1016/j.brs.2013.05.007. [PubMed: 23827648]

[64]. Elcin D, Tikidji-Hamburyan R, Canavier C. The effect of neural orientation on action potential generation elicited by transcranial magnetic stimulation: a computational study Neurosci. 2017, Soc. Neurosci. Annu. Meet, Washington, DC, USA: 2017, p. Abstract 202.04.

[65]. Tikidji-Hamburyan R PLOS Computational Biology Reader Comments: two bugs in the 2D code strongly affect results of this paper. PLoS Comput Biol 2015 https://journals.plos.org/ploscompbiol/article/comment?id=10.1371/annotation/16d77bbb-ad24-4b2a-b1df-c96847e4eed9 (accessed May 27, 2019).

[66]. Wang B, Aberra AS. PLOS Computational Biology Reader Comments: Conceptual errors and coding bugs related to how the magnetically-induced electric field is coupled to the neuron model. PLoS Comput Biol 2019 https://journals.plos.org/ploscompbiol/article/comment?id=10.1371/annotation/4e433d87-f6f6-4b87-8fac-9af31b5c2ef6 (accessed May 27, 2019).

[67]. Rattay F Analysis of Models for External Stimulation of Axons. IEEE Trans Biomed Eng 1986;BME-33:974–7. doi:10.1109/TBME.1986.325670.

[68]. Grill WM, Mortimer JT. Inversion of the Current-Distance Relationship by Transient Depolarization. IEEE Trans Biomed Eng 1997;44.

[69]. Lertmanorat Z, Durand DM. Extracellular voltage profile for reversing the recruitment order of peripheral nerve stimulation: a simulation study. J Neural Eng 2004;1:202–11. doi: 10.1088/1741-2560/1/4/003. [PubMed: 15876640]

[70]. Nowak LG, Bullier J. Axons, but not cell bodies, are activated by electrical stimulation in cortical gray matter. I. Evidence from chronaxie measurements. Exp Brain Res 1998;118:477–88. doi: 10.1007/s002210050304. [PubMed: 9504843]

[71]. Stern S, Agudelo-Toro A, Rotem A, Moses E, Neef A. Chronaxie measurements in patterned neuronal cultures from rat hippocampus. PLoS One 2015;10:1–23. doi:10.1371/journal.pone. 0132577.

[72]. Di Lazzaro V, Rothwell JC. Corticospinal activity evoked and modulated by non-invasive stimulation of the intact human motor cortex. J Physiol 2014;592:4115–28. doi:10.1113/jphysiol. 2014.274316. [PubMed: 25172954]

[73]. Krieg TD, Salinas FS, Narayana S, Fox PT, Mogul DJ. Computational and experimental analysis of TMS-induced electric field vectors critical to neuronal activation. J Neural Eng 2015;12:046014. doi:10.1088/1741-2560/12/4/046014. [PubMed: 26052136]

[74]. Aonuma S, Gomez-Tames J, Laakso I, Hirata A, Takakura T, Tamura M, et al. A high-resolution computational localization method for transcranial magnetic stimulation mapping. Neuroimage 2018;172:85–93. doi:10.1016/j.neuroimage.2018.01.039. [PubMed: 29360575]

[75]. Sakai K, Ugawa Y, Terao Y, Hanajima R, Furubayashi T, Kanazawa I. Preferential activation of different I waves by transcranial magnetic stimulation with a figure-of-eight shaped coil. Exp Brain Res 1997;113:24–32. [PubMed: 9028772]

[76]. Hamada M, Murase N, Hasan A, Balaratnam M, Rothwell JC. The role of interneuron networks in driving human motor cortical plasticity. Cereb Cortex 2013;23:1593–605. doi:10.1093/cercor/ bhs147. [PubMed: 22661405]

[77]. Shimazu H, Maier M a., Cerri G, Kirkwood P a, Lemon RN. Macaque Ventral Premotor Cortex Exerts Powerful Facilitation of Motor Cortex Outputs to Upper Limb Motoneurons. J Neurosci 2004;24:1200–11. doi:10.1523/JNEUROSCI.4731-03.2004. [PubMed: 14762138]

[78]. Tokuno H, Nambu a. Organization of nonprimary motor cortical inputs on pyramidal and nonpyramidal tract neurons of primary motor cortex: An electrophysiological study in the macaque monkey. Cereb Cortex 2000;10:58–68. [PubMed: 10639396]

[79]. Maier M a, Kirkwood P a, Brochier T, Lemon RN. Responses of single corticospinal neurons to intracortical stimulation of primary motor and premotor cortex in the anesthetized macaque monkey. J Neurophysiol 2013;109:2982–98. doi:10.1152/jn.01080.2012. [PubMed: 23536718]

[80]. Groppa S, Werner-Petroll N, Münchau A, Deuschl G, Ruschworth MFS, Siebner HR. A novel dual-site transcranial magnetic stimulation paradigm to probe fast facilitatory inputs from ipsilateral dorsal premotor cortex to primary motor cortex. Neuroimage 2012;62:500–9. doi: 10.1016/j.neuroimage.2012.05.023. [PubMed: 22626848]

[81]. Kraskov A, Prabhu G, Quallo M, Lemon R, Brochier T. Ventral premotor-motor cortex interactions in the macaque monkey during grasp: Response of single neurons to intracortical microstimulation. J Neurosci 2011;31:8812–21. doi:10.1523/JNEUROSCI.0525-11.2011. [PubMed: 21677165]

[82]. Di Lazzaro V, Restuccia D, Oliviero A, Profice P, Ferrara L, Insola A, et al. Magnetic transcranial stimulation at intensities below active motor threshold activates intracortical inhibitory circuits. Exp Brain Res 1998;119:265–8. doi:10.1007/s002210050341. [PubMed: 9535577]

[83]. Defelipe J, Conley M, Jones EG. Long-range focal collateralization of axons arising from corticocortical cells in monkey sensory-motor cortex. J Neurosci 1986;6:3749–66. [PubMed: 2432205]

[84]. Aroniadou VA, Keller A. The patterns and synaptic properties of horizontal intracortical connections in the rat motor cortex. J Neurophysiol 1993;70:1553–69. [PubMed: 7904301]

[85]. Yamashita A, Arikuni T. Axon trajectories in local circuits of the primary motor cortex in the macaque monkey (Macaca fuscata). Neurosci Res 2001;39:233–45. doi:10.1016/ S0168-0102(00)00220-0. [PubMed: 11223469]

[86]. Donoghue JP, Parham C. Afferent Connections of the Lateral Agranular Field of the Rat Motor Cortex. J Comp Neurol 1983;404:390–404.

[87]. Thomson AM, Bannister PA. Interlaminar connections in the neocortex. Cereb Cortex 2003;13:5–14. doi:10.1093/cercor/13.1.5. [PubMed: 12466210]

[88]. Bestmann S, Baudewig J, Siebner HR, Rothwell JC, Frahm J. BOLD MRI responses to repetitive TMS over human dorsal premotor cortex. Neuroimage 2005;28:22–9. doi:10.1016/j.neuroimage. 2005.05.027. [PubMed: 16002305]

[89]. Bestmann S, Baudewig J, Siebner HR, Rothwell JC, Frahm J. Functional MRI of the immediate impact of transcranial magnetic stimulation on cortical and subcortical motor circuits. Eur J Neurosci 2004;19:1950–62. doi:10.1111/j.1460-9568.2004.03277.x. [PubMed: 15078569]

[90]. Lafleur LP, Tremblay S, Whittingstall K, Lepage JF. Assessment of Effective Connectivity and Plasticity with Dual-Coil Transcranial Magnetic Stimulation. Brain Stimul 2016;9:347–55. doi: 10.1016/j.brs.2016.02.010. [PubMed: 27207765]

[91]. Di Lazzaro V, Oliviero A, Profice P, Insola A, Mazzone P, Tonali PA, et al. Direct demonstration of interhemispheric inhibition of the human motor cortex produced by transcranial magnetic stimulation. Exp Brain Res 1999;124:520–4. [PubMed: 10090664]

[92]. Rossini PM, Burke D, Chen R, Cohen LG, Daskalakis Z, Di Iorio R, et al. Non-invasive electrical and magnetic stimulation of the brain, spinal cord, roots and peripheral nerves: Basic principles and procedures for routine clinical and research application: An updated report from an I.F.C.N. Committee. Clin Neurophysiol 2015;126:1071–107. doi:10.1016/j.clinph.2015.02.001. [PubMed: 25797650]

[93]. Kujirai T, Caramia MD, Rothwell JC, Day BL, Thompson PD, Ferbert A, et al. Corticocortical inhibition in human motor cortex. J Physiol 1993;471:501–19. doi:VL - 471. [PubMed: 8120818]

[94]. Kallioniemi E, Säisänen L, Könönen M, Awiszus F, Julkunen P. On the estimation of silent period thresholds in transcranial magnetic stimulation. Clin Neurophysiol 2014;125:2247–52. doi: 10.1016/j.clinph.2014.03.012. [PubMed: 24725846]

[95]. Bestmann S, Siebner HR, Modugno N, Amassian VE, Rothwell JC. Inhibitory interactions between pairs of subthreshold conditioning stimuli in the human motor cortex. Clin Neurophysiol 2004;115:755–64. doi:10.1016/j.clinph.2003.11.002. [PubMed: 15003754]

[96]. Howell B, McIntyre CC. Analyzing the tradeoff between electrical complexity and accuracy in patient-specific computational models of deep brain stimulation. J Neural Eng 2016;13:036023. doi:10.1088/1741-2560/13/3/036023. [PubMed: 27172137]

[97]. Esser SK, Hill SL, Tononi G. Modeling the Effects of Transcranial Magnetic Stimulation on Cortical Circuits. J Neurophysiol 2005:622–39. doi:10.1152/jn.01230.2004.Modeling. [PubMed: 15788519]

[98]. Rusu CV, Murakami M, Ziemann U, Triesch J. A model of TMS-induced I-waves in motor cortex. Brain Stimul 2014;7:401–14. doi:10.1016/j.brs.2014.02.009. [PubMed: 24680789]

[99]. Opitz A, Legon W, Rowlands A, Bickel WK, Paulus W, Tyler WJ. Physiological observations validate finite element models for estimating subject-specific electric field distributions induced by transcranial magnetic stimulation of the human motor cortex. Neuroimage 2013;81:253–364. doi:10.1016/j.neuroimage.2013.04.067. [PubMed: 23644000]

[100]. Aberra AS, Wang B, Grill WM, Peterchev AV. P090 Excitation mechanisms of TMS on cortical neuron models. Clin Neurophysiol 2017;128:e52–3. doi:10.1016/j.clinph.2016.10.215.

Highlights

- Implemented multi-scale model of TMS-induced neural activation in motor cortex

- Axon morphology varied by cell type and determined dependence of activation on spatial parameters of electric field

- TMS activated with lowest intensity layer 5 pyramidal cells at their axonal terminations

- Neural activation was driven by electric field magnitude, rather than its normal component, resulting in strongest activation of superficial gyral crown/lip region

- Model predicts monophasic A–P TMS activates more anterior region of precentral gyrus than P–A TMS
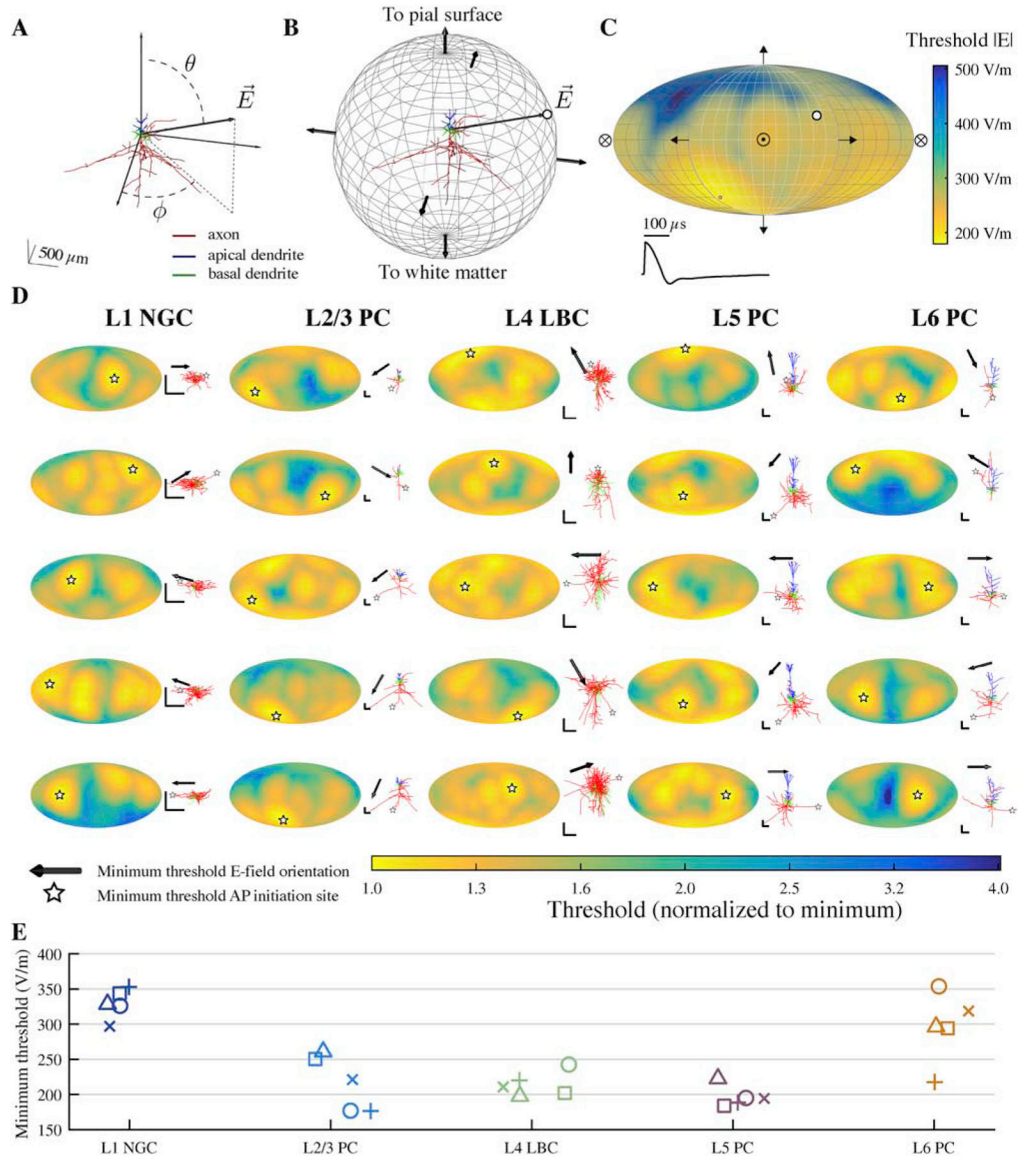
Figure 1. Threshold dependence on cell type and direction of uniform E-field.
A) Coordinate system shown for example cell (L2/3 PC). Somato-dendritic axis aligned to z-axis, with polar angle θ and azimuthal angle ϕ. **B)** Uniform E-field directions represented as normal vectors on sphere centered at origin. Thresholds were calculated for 398 directions spanning the sphere, and each threshold value was represented as a point on the sphere (white dot) corresponding to the E-field vector $\vec{E}$ **C)** 3D threshold–direction map projected into 2D using Mollweide projection. White dot indicates threshold value for example vector $\vec{E}$ in **B**, crossed circle represents E-field pointing into the page, and circle with dot represents E-field pointing out of the page. Bottom: Recorded MagPro X100 Monophasic TMS waveform. **D)** Threshold–direction maps for all cell types and their virtual clones, i.e. models of the same cell type with stochastically varied morphologies, normalized to the minimum for each clone. Within cell type, threshold–direction maps for each clone are ordered by minimum threshold, with lowest minimum threshold at the bottom. White star

denotes minimum threshold orientation. Corresponding cell morphology plotted to the right of each map with same color scheme as in **A**. Black arrow points in direction of minimum threshold orientation, matching white star. All scale bars are 250 μm. **E)** Minimum threshold for 5 clones of each cell type, grouped by layer.
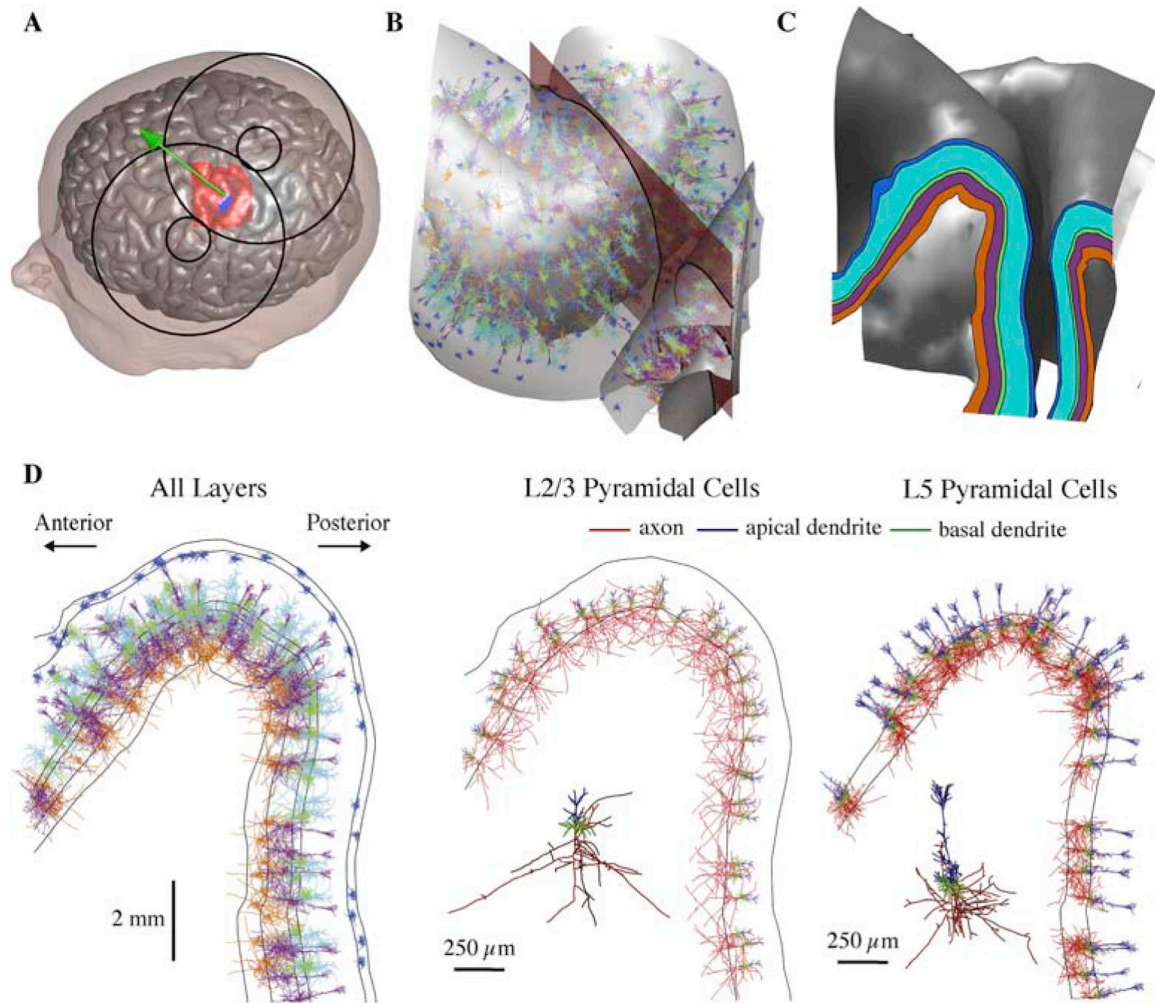
Figure 2. Embedding populations of cortical neuron models in FEM models of TMS induced E-fields.
A) Scalp and gray matter meshes are shown with the overlying TMS coil outline. The coil center and orientation are given by the green sphere and arrow, the hand knob region populated with neurons is indicated in red, and the putative hand muscle representation used in Figure 7 is shown in blue. **B)** Model neurons located in the crown of the pre-central gyrus between the gray matter and white matter surfaces. One clone from each layer is shown with color corresponding to layer (shown in **C**); five co-located model neuron populations (virtual clones of each cell type) are simulated in each layer. The 2D analysis plane (red) is used to visualize threshold data in Figure 5 and also shown in **C**–**D**. The plane is parallel to coil orientation (45° relative to midline). **C)** Cortical layers used to place and orient model neurons shown in 2D analysis plane, extracted by intersecting the analysis plane with the layer surfaces. **D)** Neural populations from **B** visualized within the 2D analysis plane. Neurons in all five layers are plotted with their respective layer colors (left). L2/3 (middle) and L5 (right) PC populations are plotted with axon, apical dendrites, and basal dendrites colored separately.
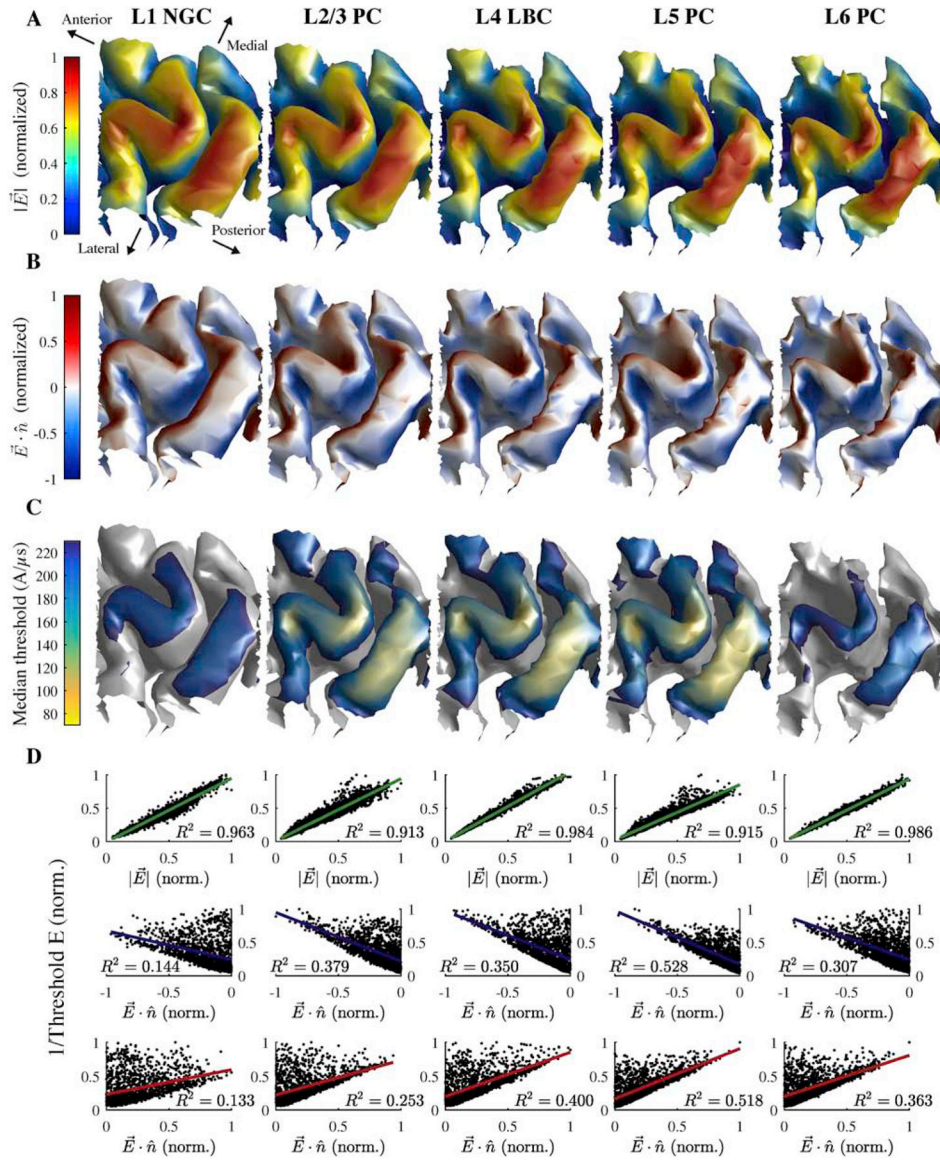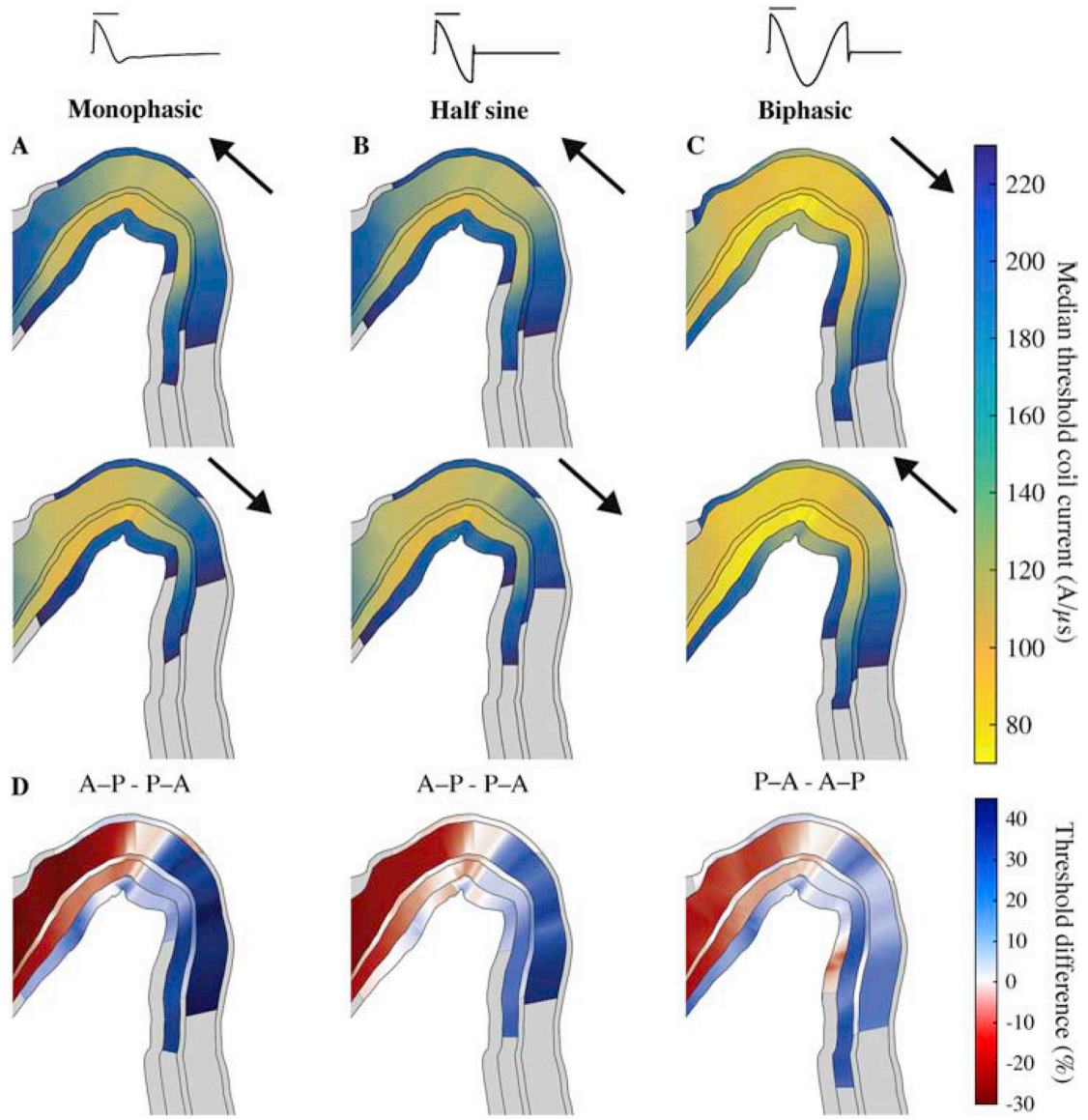
Figure 3. Layer-specific spatial distribution of activation thresholds correlate better with the E-field magnitude than normal component.
A) Magnitude of simulated E-field (normalized across layers) on layer surfaces for L1–L6 arranged adjacent to each other. **B)** Component of E-field normal to layer surfaces (normalized across layers). Positive values indicate E-field pointing out of surface and negative values indicate inward E-field. **C)** Median thresholds (across 5 clones and 6 rotations) for monophasic P–A simulation. **D)** Inverse threshold of each cell plotted against E-field magnitude (top) and absolute value of normal component (bottom) at soma, both normalized to maximum within layer (in A). Each plot includes R^2 value for linear regression of inverse threshold with corresponding E-field metric.
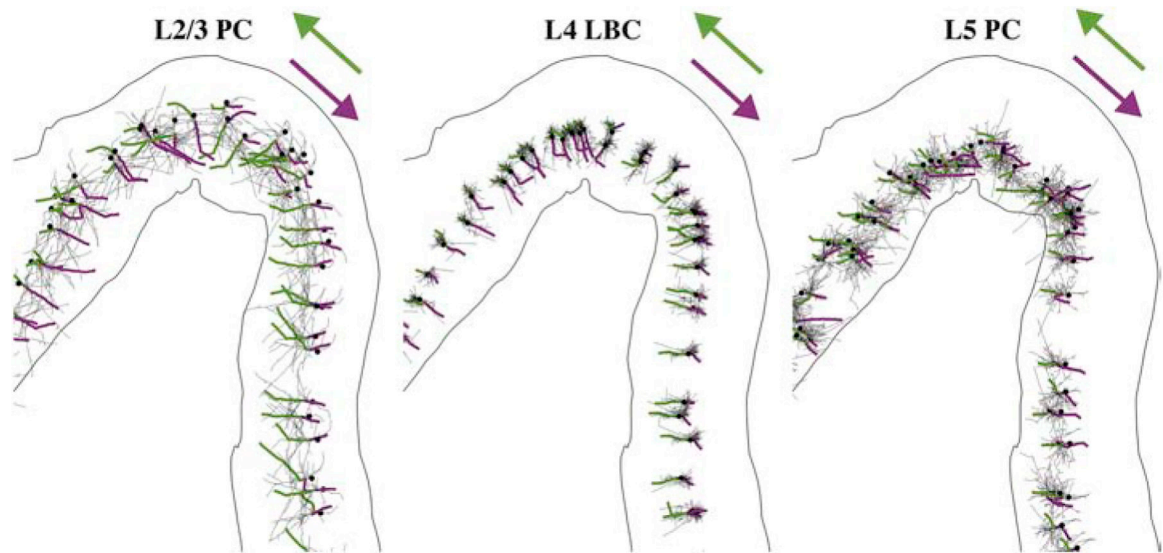
Figure 4. TMS activates axonal terminations aligned to local E-field direction.
Axonal arbors for single population of L2/3 PCs, L4 LBCs, and L5 PCs with directly activated branch colored from AP initiation point (terminal) to proximal branch point for monophasic P–A (green) and A–P (magenta) stimulation. Dendrites not shown. Somas indicated by black dots.

Figure 5. Layer-specific spatial distribution of activation varies with TMS pulse waveform and direction, shown in a cross-section of the hand knob (as in Figure 2C).

Median thresholds for L1–L6 on analysis plane through pre-central gyrus, parallel to coil handle and near coil center for **A)** monophasic, **B)** half sine, and **C)** biphasic stimulation in the P–A and A–P directions. Arrows indicate direction of initial phase of E-field waveform. Note that biphasic stimulation conditions are plotted in opposite order to group stimuli by the direction of their dominant waveform phase. **D)** Percent difference in median thresholds between P–A and A–P current directions, indicated in title. Regions where thresholds for both P–A and A–P were above 230 A/μs are colored gray.
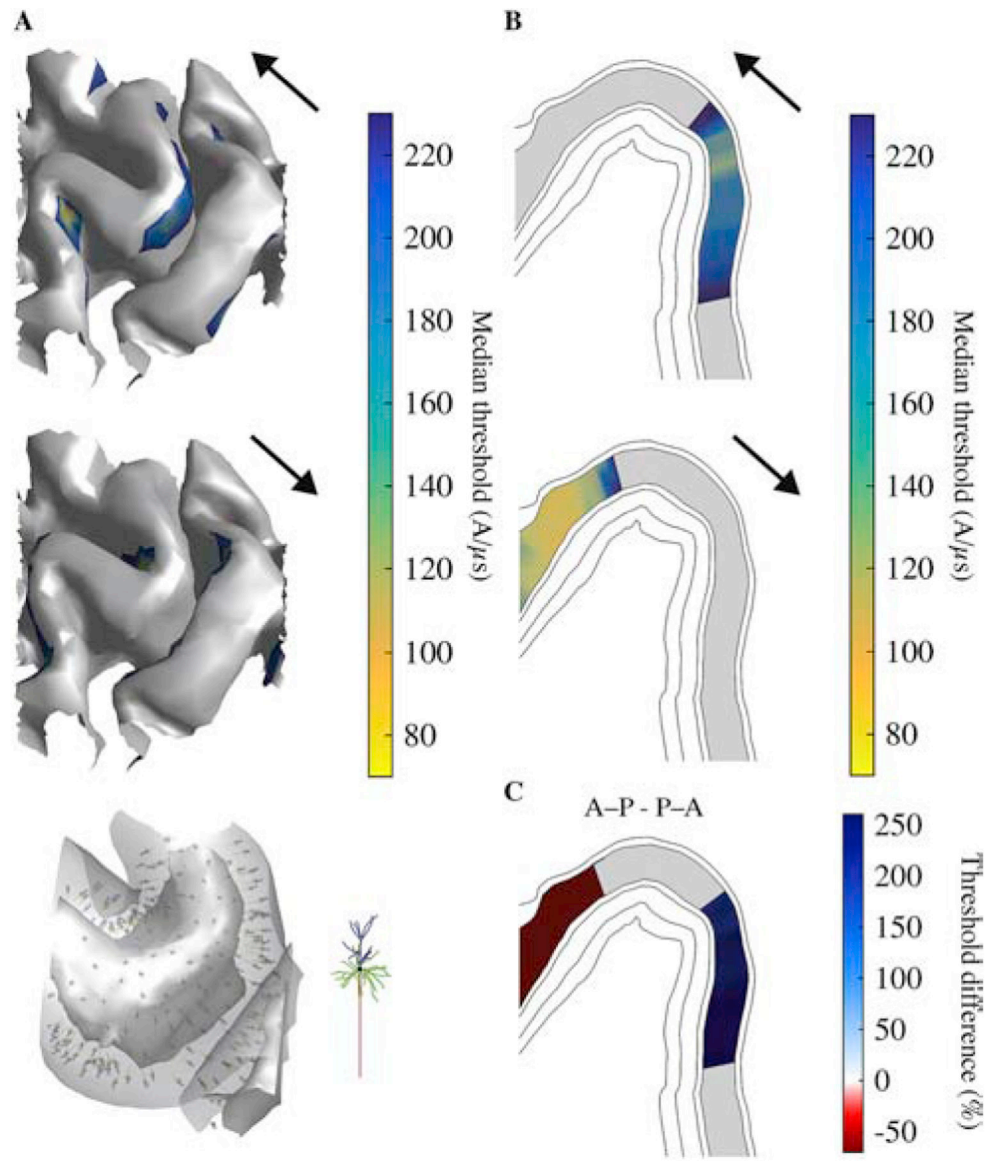
Figure 6. Simpler neuron model with straight axon morphology results in higher thresholds and different spatial distribution of activation for L2/3 PCs.
A) Median thresholds for L2/3 PCs on layer surface for monophasic P–A stimulation (top; compare to Figure 3C) and A–P stimulation (middle). Placement of L2/3 PCs with straight axons visualized in gyral crown between the gray matter and white matter surfaces (similar to Figure 2B) and zoomed in view of single model neuron (bottom). Straight axon versions of L2/3 PCs were co-located with original, realistic axon population and only differed in their axon morphology. **B)** Median thresholds for L2/3 PC on analysis plane (same as Figure 5) for monophasic P–A (top) and A–P (bottom) stimulation. **C)** Percent difference in median thresholds between P–A and A–P current directions. Regions where thresholds for both P–A and A–P were above 230 A/μs are colored gray.
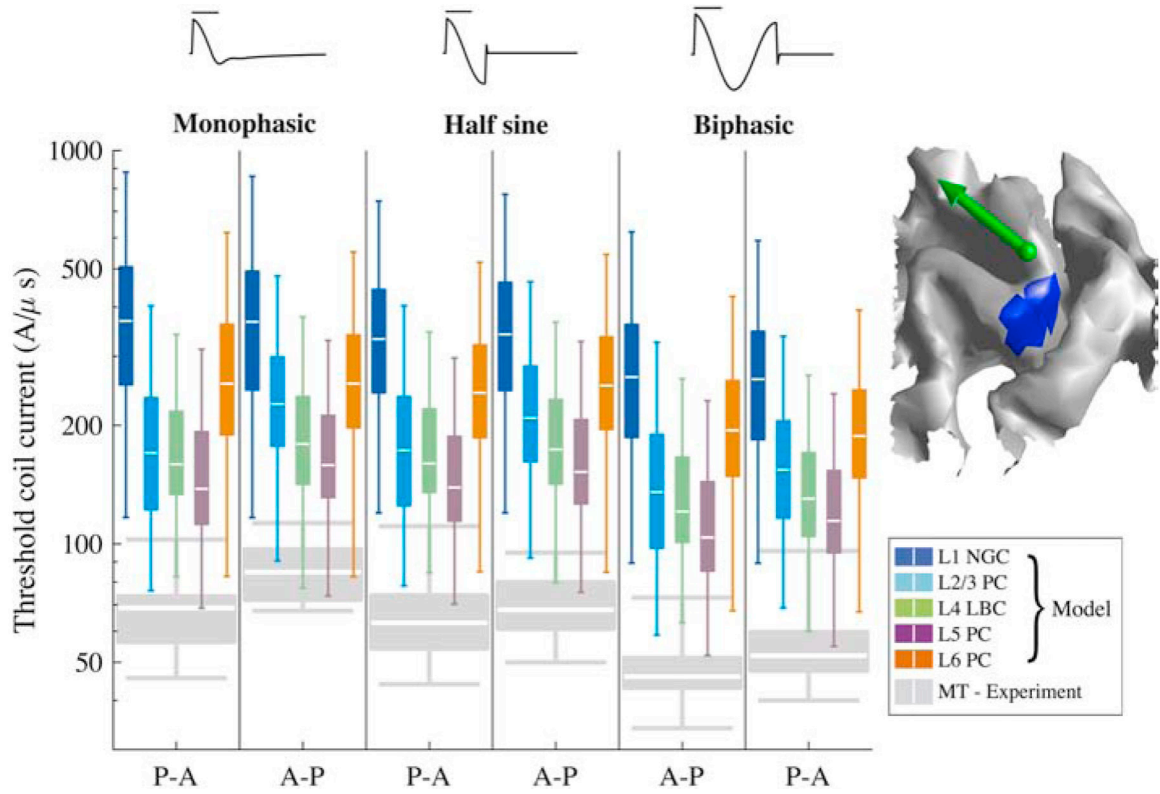
Figure 7. Activation thresholds within putative hand muscle representation in hand knob.
Model thresholds for each pulse waveform and direction combination are shown in log scale, with each Tukey boxplot (outliers excluded) describing statistics of thresholds from 5 clones and 6 rotations at each position within the hand muscle representation. Boxplots of experimental motor threshold (MT) data are included in gray (12 subjects) [41]. Hand muscle representation in L5 surface is marked in blue (right), with green arrow indicating center of TMS coil and direction of induced current (for P–A stimulation).
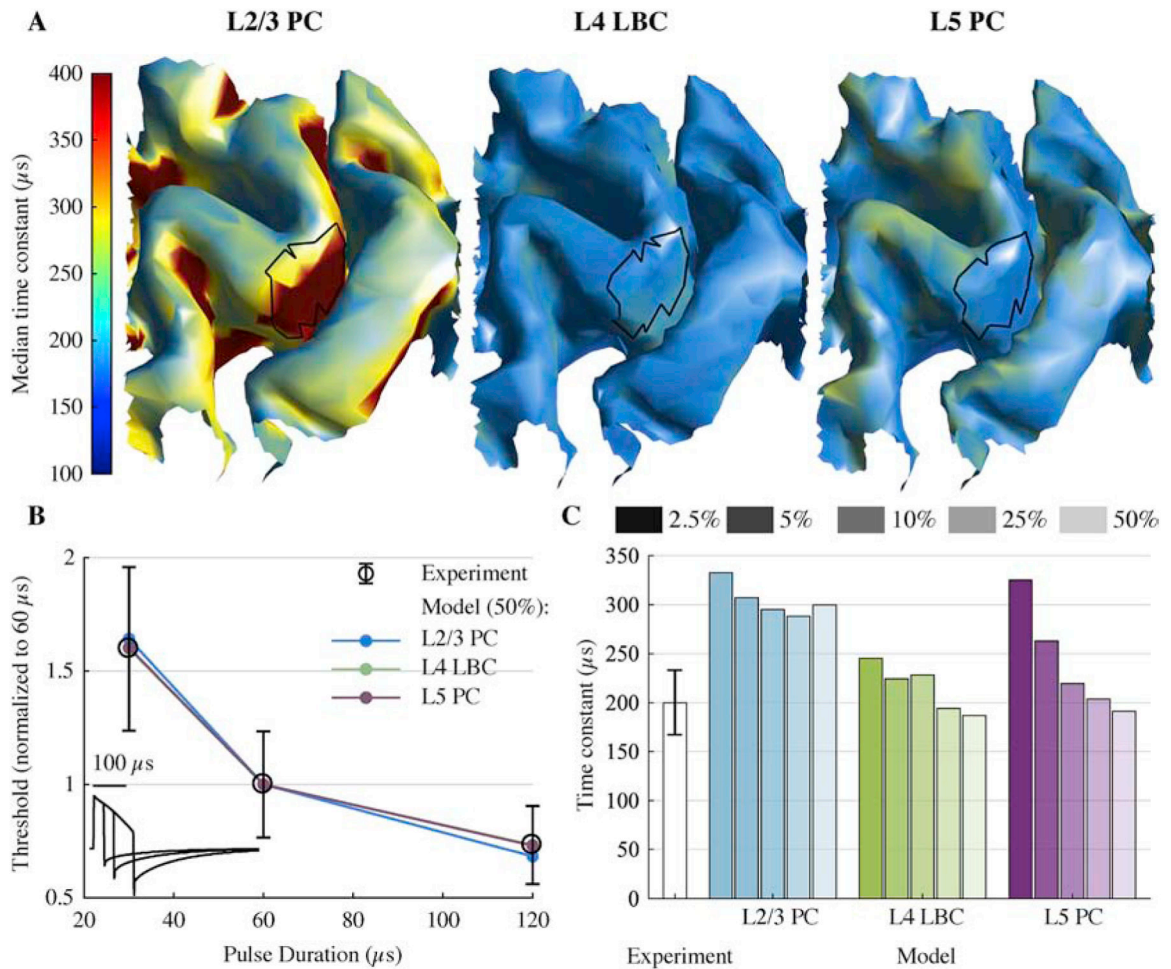
Figure 8. Strength–duration time constants of model neurons match experimental measures.
A) Median time constant (across 5 clones and 6 rotations) for layers with lowest activation thresholds, estimated for each model neuron using their activation thresholds for 30, 60, and 120 µs cTMS pulses. Putative hand muscle representations are outlined in black. **B)** Strength–duration curves using median neuronal population threshold within the model hand muscle representation and experimentally measured mean (± SD) motor thresholds [14]. cTMS waveforms are shown in the bottom left corner. **C)** Experimentally estimated time constant [14] (mean ± SD) and model time constants for a range of cutoff threshold percentiles (2.5–50%) within the hand muscle representation.